

This is the accepted manuscript made available via CHORUS. The article has been published as:

Quantum control and pathway manipulation in rubidium

Fang Gao, Yaoxiong Wang, Roberto Rey-de-Castro, Herschel Rabitz, and Feng Shuang

Phys. Rev. A **92**, 033423 — Published 29 September 2015

DOI: [10.1103/PhysRevA.92.033423](https://doi.org/10.1103/PhysRevA.92.033423)

Quantum Control and Pathway Manipulation in Rubidium

Fang Gao¹, Yaoxiong Wang^{1,2}, Roberto Rey-de-Castro³, Herschel Rabitz³, Feng Shuang^{1,2}

¹*Institute of Intelligent Machines, Chinese Academy of Sciences, Hefei 230031, China*

²*Department of Automation, University of Science and Technology of China, Hefei, 230027, China*

³*Department of Chemistry, Princeton University, Princeton, NJ 08544, USA*

(Dated: September 8, 2015)

There is an increasing interest in the extraction and control of the interfering quantum pathway amplitudes induced by control fields during laser-matter interactions. The Hamiltonian-encoding and observable-decoding (HE-OD) technique has been introduced for extracting the amplitudes of the pathways present in the dynamics and has recently been experimentally applied to the pathway manipulation of atomic Rubidium. This paper theoretically explores various strategies for manipulating pathway amplitudes in the context of a laser field interacting with a multilevel system similar to atomic Rubidium for both narrowband and broadband ultrafast fields. In the perturbation regime, two 2nd-order quantum pathways connecting the Rb states $5S_{1/2}$ and $5D_{3/2}$ dominate the dynamics, namely $5S_{1/2} \rightarrow 5P_{3/2} \rightarrow 5D_{3/2}$ (pathway 1) and $5S_{1/2} \rightarrow 5P_{1/2} \rightarrow 5D_{3/2}$ (pathway 2). For narrowband field control, the analysis is carried out in the time domain with the laser field including only four narrowband-envelope sub-pulses centered at the resonant frequencies. When the two pathways cooperate constructively, temporal oscillations appear in the ratio of the two pathway amplitudes, and we conclude in this case that the period corresponds to the detuning between transitions $5S_{1/2} \rightarrow 5P_{3/2}$ and $5P_{3/2} \rightarrow 5D_{3/2}$. For broadband field control, the dynamics are treated in the frequency domain with the laser field including both resonant and continuous non-resonant frequency components. Various control strategies based on manipulating the phase of selected spectral components are tested. Compared to the outcome from a transform limited pulse, a $\frac{\pi}{2}$ step scheme can increase the dynamic range of the ratio between the two pathway amplitudes by a factor of ~ 3 . A scheme that manipulates eight spectral blocks, in which the spectral boundaries depend on the resonant frequencies, can increase the ratio by several orders of magnitude. Numerical simulations show that further dividing the spectrum into hundreds of evenly spaced blocks does not significantly enhance the pathway ratio over the eight block scheme. The quantum control of pathways investigated in this work provides valuable insights on how to incorporate known information about the structure of quantum systems for the effective reduction of quantum control complexity.

I. INTRODUCTION

The control of quantum dynamics during laser-matter interactions is a topic of fundamental importance that also offers a wide range of potential applications. Many experimental and theoretical quantum control strategies have been proposed [1–9] including open-loop control which directly applies model-based designs to the laboratory [10], adaptive feedback control in which the control is measurement-guided [3, 11], and real-time feedback control which utilizes quantum measurement back-action on the system [12]. In the context of a multilevel quantum system, here we consider an optimum control field as inducing transitions through intermediate states to transfer population from an initial state to a target state. Each possible sequence of electronic transitions that reaches the target state constitutes a quantum pathway whose importance in the overall dynamics is quantified by a complex number referred to as a pathway amplitude [13]. In many laser experiments constructive and destructive interferences among quantum pathways are responsible for the optimal control of an observable signal. Thus, the management of quantum pathways is of fundamental importance for the outcome of quantum control experiments. The Hamiltonian-encoding-observable-decoding (HE-OD) technique [13–20] is capable of extracting the pathway amplitudes via a sequence of encoding and decoding operations. Recently, Rey-de-Castro *et al.* successfully performed such a demonstration in Rubidium vapor, and the rapidly extracted pathway amplitudes permitted steering the quantum dynamics towards a specified pathway with tailored broadband femtosecond pulses [19] obtained from an adaptive feedback control strategy. We have previously theoretically investigated the pathway dynamics for narrowband laser pulses when the target state population is maximized [21]. This paper presents a theoretical exploration of several pulse shaping strategies for manipulating quantum pathways for both narrowband and broadband laser excitation.

Silberberg *et al.* showed how a resonant two-photon absorption (TPA) process can be divided into resonant and non-resonant contributions [22]. Their experiments and supporting modelling demonstrated that the TPA yield in atomic Rb can be greatly enhanced by applying a phase shift of $\pi/2$ to a 4 nm spectral window centered on the two-photon transition frequency. The mechanism of this $\pi/2$ step phase shaping scheme is to induce constructive interferences among the quantum pathways corresponding to photon pairs in the spectral region of 8 nm around the resonant frequencies. In their work, the laser bandwidth was tuned such that the Rb system can be approximated by a three-level system with only one 2nd-order pathway ($5S_{1/2} \rightarrow 5P_{3/2} \rightarrow 5D_{3/2}$) being considered. Stowe *et al.* adopted

a similar strategy (i.e., changing the phase of a spectral window) to achieve coherent control of atomic Rb, where the contributions of both Rb pathways ($5S_{1/2} \rightarrow 5P_{3/2} \rightarrow 5D_{3/2}$ and $5S_{1/2} \rightarrow 5P_{1/2} \rightarrow 5D_{3/2}$) are considered due to much wider bandwidth of the pulse [23]. Recently, Lee *et al.* have proposed another similar scheme to simultaneously control the two pathways by manipulating the phase of eight spectral blocks for maximizing the constructive interference between the two pathways [24]. However, only the total TPA signal corresponding to the final population transferred to the Rb state $5D_{3/2}$ was investigated in the above works, and the prospect of manipulating the pathway amplitudes themselves was not discussed. Here we show how similar schemes can be applied to achieve detailed control over the quantum pathway amplitudes.

The paper is organized as follows. Section II introduces models in the time and frequency domains for narrowband and broadband field cases, respectively. Section III presents three pulse shaping schemes for manipulating quantum pathway amplitudes. Compared with transform limited (TL) pulses, an implementation of the $\frac{\Pi}{2}$ step scheme of Silberberg *et al.* can improve the amplitude ratio approximately by a factor of three, while schemes that manipulate the phase of eight or more spectral blocks are much more effective at suppressing an undesired pathway. The pathway amplitude control schemes proposed here are robust and straightforward, facilitating their prospective laboratory applications. Concluding remarks are given in Section IV.

II. THEORETICAL BACKGROUND

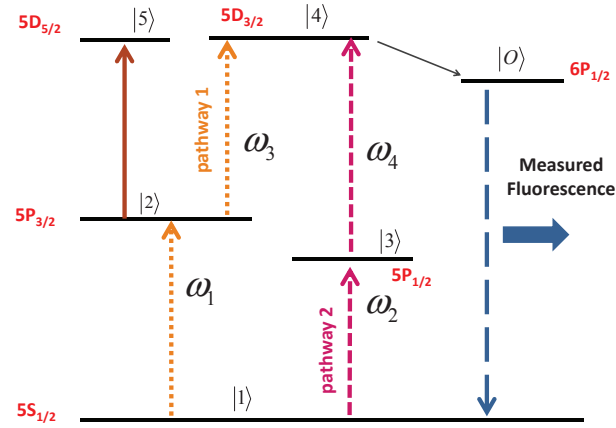


Figure 1: (Color online) Energy level diagram of atomic Rb. According to the selection rules, only transitions $|1\rangle \rightarrow |2\rangle$, $|1\rangle \rightarrow |3\rangle$, $|2\rangle \rightarrow |4\rangle$, $|2\rangle \rightarrow |5\rangle$ and $|3\rangle \rightarrow |4\rangle$ are dipole-allowed. In the laboratory, state $|4\rangle$ will decay to $|O\rangle$, and thus the population of the target state $|4\rangle$ is proportional to the measured fluorescence emitted from $|O\rangle$. Similarly, in the simulations described here the final population of state $|4\rangle$ is taken as the system's output signal.

In the dipole approximation, the Hamiltonian describing the interaction of atomic Rb with a laser field $E(t)$ is of the form $H = H_0 - \mu E(t)$, where H_0 is the field-free Hamiltonian with eigenstates $|l_p\rangle$, $p = 1, 2, \dots, 5$ and μ is the dipole moment operator. The energy level structure and dipole-allowed couplings are shown in Fig. 1. In the basis $\{|l_p\rangle\}$, $p = 1, 2, \dots, 5$, the matrices H_0 and μ are given by

$$H_0 = \begin{bmatrix} 0 & 0 & 0 & 0 & 0 \\ 0 & \omega_1 & 0 & 0 & 0 \\ 0 & 0 & \omega_2 & 0 & 0 \\ 0 & 0 & 0 & \omega_{tot} & 0 \\ 0 & 0 & 0 & 0 & \omega_{tot} \end{bmatrix},$$

$$\mu = \begin{bmatrix} 0 & \mu_{12} & \mu_{13} & 0 & 0 \\ \mu_{12} & 0 & 0 & \mu_{24} & \mu_{25} \\ \mu_{13} & 0 & 0 & \mu_{34} & 0 \\ 0 & \mu_{24} & \mu_{34} & 0 & 0 \\ 0 & \mu_{25} & 0 & 0 & 0 \end{bmatrix} \quad (1)$$

where the energy of state $|1\rangle$ is set to zero, levels $|4\rangle$ and $|5\rangle$ are degenerate, $\omega_{tot} = \omega_1 + \omega_3 = \omega_2 + \omega_4 = 0.1171$,

$\omega_1 = 0.05840$, $\omega_2 = 0.05731$, $\mu_{12} = 4.2275$, $\mu_{13} = 2.9931$, $\mu_{24} = 1.0216$, $\mu_{25} = 1.0238$, and $\mu_{34} = 0.9$ [25, 26]. Unless otherwise noted, all the quantities in this paper are given in atomic units.

The dynamics in the Schrödinger representation are described by

$$i \frac{dU(t, t_0)}{dt} = (H_0 - \mu E(t))U(t, t_0) \quad (2)$$

where t_0 is the initial time and $U(t, t_0)$ is the evolution operator. In the interaction representation the equation of motion reduces to

$$i \frac{dU_I(t, t_0)}{dt} = V_I(t)U_I(t, t_0) \quad (3)$$

where

$$V_I(t) = -\exp(iH_0 t) \mu E(t) \exp(-iH_0 t),$$

and

$$U_I(t, t_0) = \exp(iH_0 t) U(t, t_0) \exp(-iH_0 t_0).$$

In the perturbation regime, under sufficiently low laser power, the two second order pathways in Fig.1, $|1\rangle \rightarrow |2\rangle \rightarrow |4\rangle$ (pathway 1) and $|1\rangle \rightarrow |3\rangle \rightarrow |4\rangle$ (pathway 2), dominate the transfer of population from the initial state $|1\rangle$ to the target state $|4\rangle$. The amplitudes of pathways 1 and 2 are respectively given below by the two lowest-order Dyson expansion terms of $U_I(t, -\infty)$ with $t_0 = -\infty$

$$U_1(T) = -\mu_{12}\mu_{24} \int_{-\infty}^T e^{i\omega_3 t_2} E(t_2) \times \int_{-\infty}^{t_2} e^{i\omega_1 t_1} E(t_1) dt_1 dt_2, \quad (4a)$$

$$U_2(T) = -\mu_{13}\mu_{34} \int_{-\infty}^T e^{i\omega_4 t_2} E(t_2) \times \int_{-\infty}^{t_2} e^{i\omega_2 t_1} E(t_1) dt_1 dt_2 \quad (4b)$$

The final amplitudes after the pulse is over, $U_1(T)$ and $U_2(T)$ for $T \rightarrow \infty$, can be calculated from the frequency domain field $E(\omega)$ as [22]

$$U_1(T \rightarrow \infty) = \mu_{12}\mu_{24} [-\pi E(\omega_1) E(\omega_3) + i\wp \int_{-\infty}^{\infty} \frac{E(\omega) E(\omega_{41} - \omega)}{\omega_1 - \omega} d\omega], \quad (5a)$$

$$U_2(T \rightarrow \infty) = \mu_{13}\mu_{34} [-\pi E(\omega_2) E(\omega_4) + i\wp \int_{-\infty}^{\infty} \frac{E(\omega) E(\omega_{41} - \omega)}{\omega_2 - \omega} d\omega] \quad (5b)$$

where \wp is the Cauchy principal value, and $\omega_{41} = \omega_1 + \omega_3 = \omega_2 + \omega_4$, which corresponds to the energy difference between states $|4\rangle$ and $|1\rangle$. The output signal here is taken as the total transition probability from the initial state $|1\rangle$ to the target state $|4\rangle$ after the pulse and is given by

$$P_{41} = |\langle 4 | U_I(T, 0) | 1 \rangle|^2 \approx |U_1(T) + U_2(T)|_{T \rightarrow \infty}^2 \quad (6)$$

III. PATHWAY CONTROL STRATEGIES

The pathway dynamics may be manipulated by changing the phases and amplitudes of the various frequency components in the control field $E(\omega)$, as implied by Eqs. (5a) and (5b). In this section we investigate pathway control

strategies using both narrowband and broadband controls. In the narrowband control cases, the field consists of a discrete sum of a few narrow-band resonant spectral components, and the quantum state is propagated according to Eq. (3) for several laser intensities varying from weak to strong. In the broadband control cases, non-resonant frequencies are also considered in the control field which corresponds to an ultrafast laser field with a continuous spectrum. The quantum dynamics are more complex in the latter cases, and Eq. (5) in the frequency domain is utilized to treat the dynamics perturbatively.

A. Narrowband field cases

In the narrowband regime, the laser field is written in the time domain with a Gaussian envelope :

$$E(t) = \exp(-(t - t_{1/2})^2/\Delta^2) \times \sum_{k=1}^4 A_k \cos(\omega_k t + \varphi_k)$$

where the target time T is taken to be large enough to ensure that the entire pulse interacts with the system before the population transfer signal is recorded, $t_{1/2}$ lies at the center of the pulse's time span, and $\Delta = 1/\sqrt{\ln 2}$ ps. Thus, the field corresponds to a pulse with a temporal full width at half maximum (FWHM) of 2 ps. In our simulations, eight parameters ($A_1, A_2, A_3, A_4, \varphi_1, \varphi_2, \varphi_3, \varphi_4$) are optimized to maximize the population transfer $P_{41} = |\langle 4|U(T, 0)|1\rangle|^2$ from the initial state $|1\rangle$ to the target state $|4\rangle$ at the final time T . A genetic algorithm (GA) is employed to search for fields that optimally manipulate the quantum pathways.

The focus here is on manipulating the ratio between the two pathway amplitudes, since in the laboratory it is more feasible to measure the pathway ratio instead of their absolute individual values [19]. For the conditions specified in Sec. II in the weak field regime, U_1 and U_2 have a similar magnitude under an optimal laser field for maximizing total population transfer [21]. When the two pathways cooperate to achieve maximum population transfer, one important observed feature is the appearance of temporal oscillations in the ratio $|U_1/U_2|$ [21]. The temporal dependence of the ratio $|U_1(t)/U_2(t)|$ can be extracted in the laboratory by combining HE-OD with a laser pulse truncation procedure [20]. An experimentally observed oscillation of the ratio with a period of ~ 500 fs was found under the conditions of broadband control. A similar oscillation feature was also identified by an analytical treatment with a narrow-bandwidth rectangular control pulse [21], even though the control field was qualitatively different from the experimental broadband laser pulse [20]. Here we will show that a similar oscillation appears when considering a more realistic Gaussian envelope in the control field. As shown in Fig. 2, when the upper limit of the four spectral amplitudes is set as 2.5×10^{-5} , the ratio oscillates with a period ~ 500 fs. In the following, this behavior will be assessed within an analytical model considering the envelope of the laser field. In the rotating wave approximation, we have

$$\begin{aligned} U_1(t) &= -\frac{\mu_{12}\mu_{24}}{4} \sum_{p,q}^4 \int_{-\infty}^t e^{i\omega_3 t_2} \exp(-(t_2 - t_{1/2})^2/\Delta^2) \\ &\quad \times A_q e^{-i(\omega_q t_2 + \varphi_q)} \int_{-\infty}^{t_2} e^{i\omega_1 t_1} \exp(-(t_1 - t_{1/2})^2/\Delta^2) \\ &\quad \times A_p e^{-i(\omega_p t_1 + \varphi_p)} dt_1 dt_2 \\ &= -\frac{\mu_{12}\mu_{24}}{4} \sum_{p,q}^4 A_p A_q U_{pq}^{(13)}(t), \end{aligned} \tag{7a}$$

$$\begin{aligned} U_2(t) &= -\frac{\mu_{13}\mu_{34}}{4} \sum_{p,q}^4 \int_{-\infty}^t e^{i\omega_4 t_2} \exp(-(t_2 - t_{1/2})^2/\Delta^2) \\ &\quad \times A_q e^{-i(\omega_q t_2 + \varphi_q)} \int_{-\infty}^{t_2} e^{i\omega_2 t_1} \exp(-(t_1 - t_{1/2})^2/\Delta^2) \\ &\quad \times A_p e^{-i(\omega_p t_1 + \varphi_p)} dt_1 dt_2 \\ &= -\frac{\mu_{13}\mu_{34}}{4} \sum_{p,q}^4 A_p A_q U_{pq}^{(24)}(t) \end{aligned} \tag{7b}$$

with

$$\begin{aligned}
U_{pq}^{(mn)}(t) &= \int_{-\infty}^t e^{i\omega_n t_2} \exp(-(t_2 - t_{1/2})^2 / \Delta^2) e^{-i(\omega_q t_2 + \varphi_q)} dt_2 \\
&\times \int_{-\infty}^{t_2} e^{i\omega_m t_1} \exp(-(t_1 - t_{1/2})^2 / \Delta^2) \\
&\times e^{-i(\omega_p t_1 + \varphi_p)} dt_1
\end{aligned}$$

Assuming that all amplitudes (A_k) have approximately the same magnitude, then the following results can be derived by keeping only the largest (U_{13}^{13} and U_{24}^{24}) and second largest terms (U_{11}^{13} , U_{31}^{13} , U_{13}^{24} and U_{23}^{24})

$$U_1(t) \approx -\frac{\mu_{12}\mu_{24}}{4} (A_1 A_3 U_{13}^{13} + A_1 A_1 U_{11}^{13} + A_3 A_1 U_{31}^{13}),$$

$$U_2(t) \approx -\frac{\mu_{13}\mu_{34}}{4} (A_2 A_4 U_{24}^{24} + A_1 A_3 U_{13}^{24} + A_2 A_3 U_{23}^{24})$$

where

$$|U_{13}^{13}| = |U_{24}^{24}| = \int_{-\infty}^T e^{-\frac{(t_2 - t_{1/2})^2}{\Delta^2}} \int_{-\infty}^{t_2} e^{-\frac{(t_1 - t_{1/2})^2}{\Delta^2}} dt_1 dt_2 \quad (8)$$

Since for the narrowband field considered here the detunings $\omega_{pq} = \omega_p - \omega_q$ are much larger than the bandwidth $1/\Delta$ (e.g., $\omega_{31} \gg 1/\Delta$), then we have that

$$U_{11}^{13} \approx \frac{-ie^{-\frac{(t - t_{1/2})^2}{\Delta^2}} e^{i\omega_{31}T}}{\omega_3 - \omega_1} \int_{-\infty}^T e^{-\frac{(t - t_{1/2})^2}{\Delta^2}} e^{-2i\varphi_1} dt, \quad (9)$$

$$U_{31}^{13} \approx \frac{i \int_{-\infty}^T e^{-\frac{(t - t_{1/2})^2}{\Delta^2}} e^{-i(\varphi_1 + \varphi_3)} dt}{\omega_3 - \omega_1}, \quad (10)$$

$$U_{13}^{24} \approx \frac{i \int_{-\infty}^T e^{-\frac{(t - t_{1/2})^2}{\Delta^2}} e^{-i(\varphi_1 + \varphi_3)} dt}{\omega_4 - \omega_3},$$

$$U_{23}^{24} \approx \frac{-ie^{-\frac{(t - t_{1/2})^2}{\Delta^2}} e^{i\omega_{43}T}}{\omega_4 - \omega_3} \int_{-\infty}^T e^{-\frac{(t - t_{1/2})^2}{\Delta^2}} e^{-2i(\varphi_2 + \varphi_3)} dt$$

Due to the fact that $\omega_4 - \omega_3 \gg \omega_3 - \omega_1$, the second largest terms of $U_2(t)$ (U_{13}^{24} and U_{23}^{24}) have much smaller magnitude than those of $U_1(t)$ (U_{11}^{13} and U_{31}^{13}), which leads to

$$\begin{aligned}
\frac{U_1(t)}{U_2(t)} &\approx \frac{\mu_{12}\mu_{24} (A_1 A_3 U_{13}^{13} + A_1 A_1 U_{11}^{13} + A_3 A_1 U_{31}^{13})}{\mu_{13}\mu_{34} (A_2 A_4 U_{24}^{24} + A_1 A_3 U_{13}^{24} + A_2 A_3 U_{23}^{24})} \\
&\approx \frac{\mu_{12}\mu_{24} (A_1 A_3 U_{13}^{13} + A_1 A_1 U_{11}^{13} + A_3 A_1 U_{31}^{13})}{\mu_{13}\mu_{34} A_2 A_4 U_{24}^{24}} \\
&= \frac{\mu_{12}\mu_{24} A_1 A_3}{\mu_{13}\mu_{34} A_2 A_4} e^{i(\varphi_2 + \varphi_4 - \varphi_1 - \varphi_3)} \\
&\quad + \frac{\mu_{12}\mu_{24} (A_1 A_1 U_{11}^{13} + A_3 A_1 U_{31}^{13})}{\mu_{13}\mu_{34} A_2 A_4 U_{24}^{24}} \quad (11)
\end{aligned}$$

From Eqs. (8-11), we can see that the ratio $|U_1(t)/U_2(t)|$ has a period $\sim 2\pi/(\omega_3 - \omega_1) \sim 500fs$. This behavior is also evident in Fig. 2. This analysis is in agreement with the conclusions drawn in our previous work [21] where a rectangular pulse envelope was employed. Thus, under narrowband excitation, oscillations in the pathway ratio can be explained as a result of the detunings between the transition frequencies.

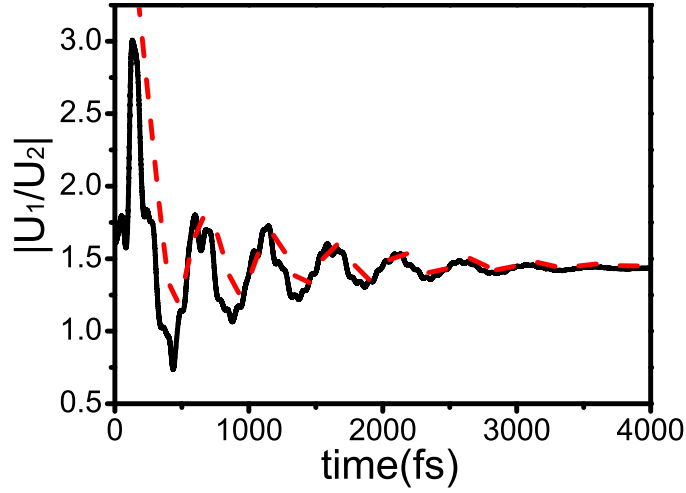


Figure 2: (Color online) The amplitude ratio $|U_1/U_2|$ computed with Eq. (7) (black solid line) and Eq. (11) (red dashed line).

B. Broadband field cases

The analysis above reveals features of the control mechanism in the narrowband regime. On the other hand, laboratory quantum control fields are often broadband (e.g., as in ultrafast laser control), including both resonant and continuous non-resonant frequencies. The dynamics of the controlled system under broadband excitation will generally be more complex than in narrowband field control. In this section, a broadband field with weak intensity is applied to control the same quantum system. In this case, as will become apparent below, working in the frequency domain is more suitable for revealing the control mechanism. The laser field in the frequency domain is assumed to be:

$$E(\omega) = E_0 \times \exp(-(\omega - \omega_0)^2 / \Delta^2) \times e^{i\varphi(\omega)}$$

where the pulse's central wavelength $\lambda_0 = 2\pi c/\omega_0$ and FWHM are 782 nm and 45 nm, respectively. These field parameters were chosen to approach the experimental conditions in Ref. [24]. In our simulations, E_0 is taken to be 0.0006 (a.u.), well within the perturbative regime, and only the phase $\varphi(\omega)$ is adjusted in the optimizations.

The frequency domain is divided into evenly spaced blocks of spectral width d . Below, in both the eight-block scheme and multi-block scheme A, the phases of the blocks $(\omega_{reson} - \frac{d}{2}, \omega_{reson} + \frac{d}{2})$ centered at the resonant frequencies ω_{reson} are fixed to zero.

1. $\frac{\pi}{2}$ Step Scheme

As mentioned above, Silberberg *et al.* [22] proposed a $\frac{\pi}{2}$ step scheme to increase the two-photon absorption (TPA) rate, in which a phase shift of $\frac{\pi}{2}$ was applied to a spectral window with a width equal to the frequency difference of the two resonant transitions and centered at half the energy gap between the initial and target states. Pathways 1 and 2 can each be seen as a separate TPA process. Therefore, the $\frac{\pi}{2}$ step scheme is a natural choice to maximize them separately: the spectral window with a phase shift of $\pi/2$ is applied to the pulse, and its width is set to be $|\omega_3 - \omega_1|$ to maximize the amplitude of pathway 1 ($|U_1|$) and similarly $|\omega_4 - \omega_2|$ in order to maximize the amplitude of pathway 2 ($|U_2|$), respectively. Figure 3 shows that, when the window is centered at $\frac{\omega_1 + \omega_3}{2}$, the amplitudes of pathways 1 (bottom panel) and 2 (top panel) both achieve their maxima, with the ratio $|U_1/U_2|$ and $|U_2/U_1|$ approximately to be 7.9908 and 1.3816, respectively. Compared with the corresponding values ($|U_1/U_2| = 2.0744$; $|U_2/U_1| = 1/2.0744 = 0.4821$) for TL pulses, the $\frac{\pi}{2}$ step scheme can increase the ratio between the two pathway amplitudes approximately by a factor of three. The $\frac{\pi}{2}$ step scheme implemented here only maximizes the individual pathway amplitudes and does not consider the interference between the two pathways, which may further improve the pathway ratios $|U_1/U_2|$ or $|U_2/U_1|$.

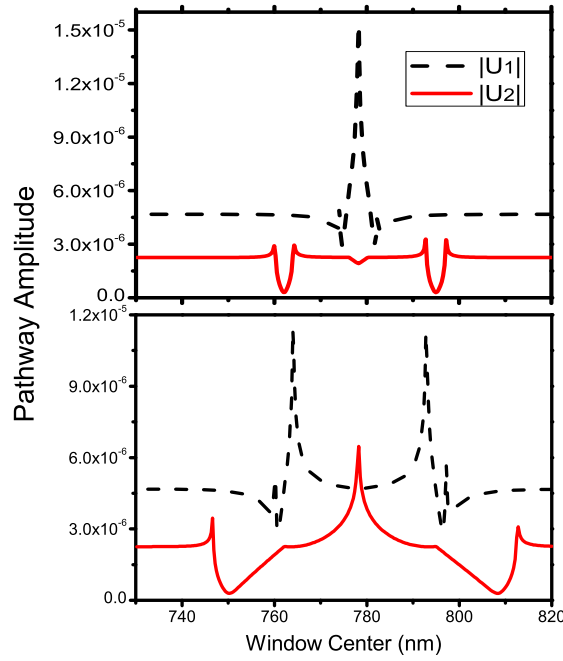


Figure 3: (Color online) In the $\frac{\pi}{2}$ step scheme, the spectral window is scanned over the pulse's spectrum. Here the spectral window widths are taken to be $|\omega_4 - \omega_2|$ (top panel) and $|\omega_3 - \omega_1|$ (bottom panel), respectively.

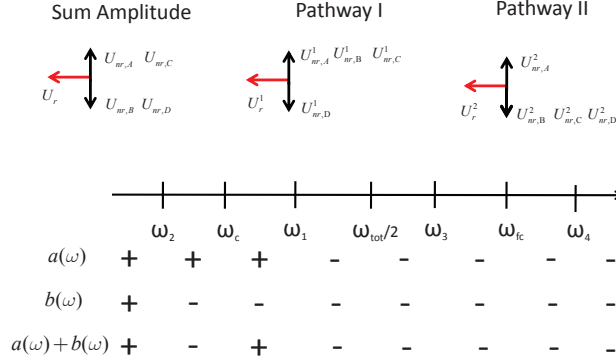


Figure 4: (Color online) In the eight-block scheme, the pulse's spectrum is divided into eight blocks, with the seven boundaries ω_2 , $\omega_c = \frac{k\omega_1 + \omega_2}{k+1}$, ω_1 , $\frac{\omega_{tot}}{2}$, ω_3 , $\omega_{fc} = \omega_1 + \omega_3 - \omega_c$ and ω_4 [24], where $k = \frac{\mu_{12}\mu_{24}}{\mu_{13}\mu_{34}}$. The spectral blocks are labelled with an integer index $j = 1, 2, \dots, 8$ with increasing frequency. The contributing terms of $U_1 (T \rightarrow \infty) + U_2 (T \rightarrow \infty)$, $U_1 (T \rightarrow \infty)$ and $U_2 (T \rightarrow \infty)$ are drawn in the complex plane in the top panel. Here $U_r = U_r^1 + U_r^2$. For a TL pulse, the non-resonant terms of U_{nr}^1 , U_{nr}^2 and U_{nr} can all be decomposed into four parts (A, B, C and D), with each part integrated in two paired spectral blocks, as shown in Eqs. (13), (14) and (15), respectively. For example, A corresponds to blocks 1 and 8. The signs of $a(\omega)$, $b(\omega)$ and $a(\omega) + b(\omega)$ given in the bottom panel. It can be seen that $a(\omega) + b(\omega)$ in the neighboring blocks changes to the opposite sign when $\omega < \omega_{tot}/2$. The conditions to maximize $|U_1|$, $|U_2|$ and $|U_1 + U_2|$ can be easily extracted: Case I, $\varphi_1 = -\frac{\pi}{2}$ and $\varphi_2 = \varphi_3 = \varphi_4 = \frac{\pi}{2}$ for $|U_1|$ maximization; Case II, $\varphi_1 = \varphi_2 = \varphi_3 = -\frac{\pi}{2}$ and $\varphi_4 = \frac{\pi}{2}$ for $|U_2|$ maximization. Case III, $\varphi_1 = \varphi_3 = \frac{\pi}{2}$ and $\varphi_2 = \varphi_4 = -\frac{\pi}{2}$ for $|U_1 + U_2|$ maximization [24].

2. Eight-Block Scheme

As mentioned above, Lee *et al.* [24] proposed an eight-block scheme to increase the total TPA yield of atomic Rubidium. In their work, the laser's spectrum is divided into eight blocks corresponding to the sign-shifted non-resonant terms in Eq. (5). The eight-block scheme is applied here to investigate the quantum pathway manipulation in Rubidium. In this scheme, the phases at the resonant frequencies, ω_1 , ω_2 , ω_3 and ω_4 , are fixed to zero, and the amplitudes of pathways 1 and 2 are given by:

Objective functions				
$ U_1 $ (Case I)	$ U_2 $ (Case II)	$ U_1 + U_2 $ (Case III)	$\frac{ U_1 }{ U_2 +cons}$ (Case IV)	$\frac{ U_2 }{ U_1 +cons}$ (Case V)
0.5073π	0.5089π	0.5077π	0.1409π	0.8863π
0.5073π	-0.4911π	-0.4923π	0.1894π	-0.2997π
0.5073π	-0.4911π	0.5077π	0.5733π	-0.0503π
-0.4927π	-0.4911π	-0.4923π	-0.4934π	0.1476π
1.958×10^{-5}	5.209×10^{-6}	1.933×10^{-5}	1.938×10^{-5}	5.654×10^{-13}
7.700×10^{-8}	7.708×10^{-6}	5.567×10^{-6}	1.543×10^{-12}	6.748×10^{-6}
1.966×10^{-5}	1.292×10^{-5}	2.489×10^{-5}	1.938×10^{-5}	6.748×10^{-6}

Table I: The optimization results under different objective functions. Here $cons. = 10^{-8}$ is introduced to avoid a singular result. The first four rows correspond to the four phases φ_1 , φ_2 , φ_3 and φ_4 , respectively, while the last three rows denote the values of $|U_1|$, $|U_2|$ and $|U_1 + U_2|$, respectively.

$$\begin{aligned}
U_1(T \rightarrow \infty) &= U_r^1 + U_{nr}^1 \\
&= -\pi\mu_{12}\mu_{24}E(\omega_1)E(\omega_3) \\
&\quad + i\mu_{12}\mu_{24}\oint_{-\infty}^{\infty} a(\omega) d\omega,
\end{aligned} \tag{12a}$$

$$\begin{aligned}
U_2(T \rightarrow \infty) &= U_r^2 + U_{nr}^2 \\
&= -\pi\mu_{13}\mu_{34}E(\omega_2)E(\omega_4) \\
&\quad + i\mu_{13}\mu_{34}\oint_{-\infty}^{\infty} b(\omega) d\omega
\end{aligned} \tag{12b}$$

with

$$a(\omega) = \frac{E(\omega)E(\omega_{41} - \omega)}{\omega_1 - \omega}, \quad b(\omega) = \frac{E(\omega)E(\omega_{41} - \omega)}{\omega_2 - \omega}$$

Here U_r^1 and U_r^2 correspond, respectively, to the resonant terms in Eqs. (12a) and (12b), while U_{nr}^1 and U_{nr}^2 refer, respectively, to the non-resonant integral terms in Eqs. (12a) and (12b). As shown in Fig. 4, the integral kernel of U_{nr} , i.e., $a(\omega) + b(\omega)$, changes to the opposite sign for TL pulses in the neighboring blocks when $\omega < \omega_{tot}/2$. If the eight blocks are labelled as $j = 1, 2, \dots, 8$, then the non-resonant terms will only depend on the sum of phase pairs $\varphi_j + \varphi_{9-j}$ with φ_j being the phase for the j th block:

$$\begin{aligned}
U_{nr}^1 &= i\mu_{12}\mu_{24} \left[\left(\int_1 |a(\omega)| d\omega - \int_8 |a(\omega)| d\omega \right) e^{i(\varphi_1 + \varphi_8)} \right. \\
&\quad + \left(\int_2 |a(\omega)| d\omega - \int_7 |a(\omega)| d\omega \right) e^{i(\varphi_2 + \varphi_7)} \\
&\quad + \left(\int_3 |a(\omega)| d\omega - \int_6 |a(\omega)| d\omega \right) e^{i(\varphi_3 + \varphi_6)} \\
&\quad \left. - \left(\int_4 |a(\omega)| d\omega + \int_5 |a(\omega)| d\omega \right) e^{i(\varphi_4 + \varphi_5)} \right] \\
&= U_{nr,A}^1 e^{i(\varphi_1 + \varphi_8)} + U_{nr,B}^1 e^{i(\varphi_2 + \varphi_7)} \\
&\quad + U_{nr,C}^1 e^{i(\varphi_3 + \varphi_6)} + U_{nr,D}^1 e^{i(\varphi_4 + \varphi_5)},
\end{aligned} \tag{13}$$

$$\begin{aligned}
U_{nr}^2 &= i\mu_{13}\mu_{34} \left[\left(\int_1 |b(\omega)| d\omega - \int_8 |b(\omega)| d\omega \right) e^{i(\varphi_1+\varphi_8)} \right. \\
&\quad - \left(\int_2 |b(\omega)| d\omega + \int_7 |b(\omega)| d\omega \right) e^{i(\varphi_2+\varphi_7)} \\
&\quad - \left(\int_3 |b(\omega)| d\omega + \int_6 |b(\omega)| d\omega \right) e^{i(\varphi_3+\varphi_6)} \\
&\quad \left. - \left(\int_4 |b(\omega)| d\omega + \int_5 |b(\omega)| d\omega \right) e^{i(\varphi_4+\varphi_5)} \right] \\
&= U_{nr,A}^2 e^{i(\varphi_1+\varphi_8)} + U_{nr,B}^2 e^{i(\varphi_2+\varphi_7)} \\
&\quad + U_{nr,C}^2 e^{i(\varphi_3+\varphi_6)} + U_{nr,D}^2 e^{i(\varphi_4+\varphi_5)}
\end{aligned} \tag{14}$$

Here U_{nr}^1 are U_{nr}^2 are dependent only on the first four phases because the last four phases may be set to zero without loss of generality. When all the phases are set to zero (i.e., for a TL pulse controlling the dynamics), $U_{nr,M}^1$ and $U_{nr,M}^2$ ($M = A, B, C, D$) are defined as the resulting non-resonant contributions integrated in two paired blocks for pathways 1 and 2, respectively. For instance, $U_{nr,A}^1$ is integrated in blocks 1 and 8.

Thus, the summation of the non-resonant terms is

$$\begin{aligned}
U_{nr} &= U_{nr}^1 + U_{nr}^2 \\
&= i(\mu_{12}\mu_{24} \int_1 |a(\omega)| d\omega - \mu_{12}\mu_{24} \int_8 |a(\omega)| d\omega \\
&\quad + \mu_{13}\mu_{34} \int_1 |b(\omega)| d\omega - \mu_{13}\mu_{34} \int_8 |b(\omega)| d\omega) e^{i(\varphi_1+\varphi_8)} \\
&\quad - i(\mu_{13}\mu_{34} \int_2 |b(\omega)| d\omega + \mu_{13}\mu_{34} \int_7 |b(\omega)| d\omega \\
&\quad - \mu_{12}\mu_{24} \int_2 |a(\omega)| d\omega + \mu_{12}\mu_{24} \int_7 |a(\omega)| d\omega) e^{i(\varphi_2+\varphi_7)} \\
&\quad + i(\mu_{12}\mu_{24} \int_3 |a(\omega)| d\omega - \mu_{12}\mu_{24} \int_6 |a(\omega)| d\omega \\
&\quad - \mu_{13}\mu_{34} \int_3 |b(\omega)| d\omega + \mu_{13}\mu_{34} \int_6 |b(\omega)| d\omega) e^{i(\varphi_3+\varphi_6)} \\
&\quad - i(\mu_{13}\mu_{34} \int_4 |b(\omega)| d\omega + \mu_{13}\mu_{34} \int_5 |b(\omega)| d\omega \\
&\quad - \mu_{12}\mu_{24} \int_4 |a(\omega)| d\omega + \mu_{12}\mu_{24} \int_5 |a(\omega)| d\omega) e^{i(\varphi_4+\varphi_5)} \\
&= U_{nr,A} e^{i(\varphi_1+\varphi_8)} + U_{nr,B} e^{i(\varphi_2+\varphi_7)} \\
&\quad + U_{nr,C} e^{i(\varphi_3+\varphi_6)} + U_{nr,D} e^{i(\varphi_4+\varphi_5)}
\end{aligned} \tag{15}$$

Here $U_{nr,M}$ ($M = A, B, C, D$) is just the sum of $U_{nr,M}^1$ and $U_{nr,M}^2$. Within each parenthesis in Eqs. (13-15), the first term is dominant leading to the conditions depicted in the diagram at the top panel of Fig. 4. In the numerical simulations, a finite difference-based gradient method is employed to seek an optimal control for five cases with different objectives. For consistency, the same fitness functions were tried in all the control strategies considered here, the results in Table I show that the magnitude of the desired pathway is the same as its maximal value in the first two fitnesses (i.e., fitness equal to $|U_1|$ or $|U_2|$), while the amplitude of the other pathway is suppressed by several orders of magnitude. For example, the amplitudes of pathway 2 are respectively 6.748×10^{-6} and 7.708×10^{-6} in cases V and II, while those of pathway 1 are 5.654×10^{-13} and 1.958×10^{-5} , respectively. Compared with a TL pulse, the pathway ratio ($|U_1|/|U_2|$ or $|U_2|/|U_1|$) is improved approximately by a factor of 10^7 . Therefore, the eight-block scheme can effectively manipulate quantum control pathways by changing only four phase variables $\varphi_1, \varphi_2, \varphi_3$ and φ_4 , a situation that may be ideal for laboratory applications.

Objective functions	Control Schemes			
	$\frac{11}{2}$ Step Scheme	Eight-block Scheme	Multi-block Scheme A	Multi-block Scheme B
$ U_1 $	$1.533 \times 10^{-5}, 1.918 \times 10^{-6}$	$1.958 \times 10^{-5}, 7.700 \times 10^{-8}$	$2.237 \times 10^{-5}, 2.787 \times 10^{-6}$	$1.994 \times 10^{-5}, 2.038 \times 10^{-6}$
$ U_2 $	$4.685 \times 10^{-6}, 6.473 \times 10^{-6}$	$5.209 \times 10^{-6}, 7.708 \times 10^{-6}$	$4.966 \times 10^{-6}, 7.857 \times 10^{-6}$	$4.658 \times 10^{-6}, 7.140 \times 10^{-6}$
$ U_1 + U_2 $		$1.933 \times 10^{-5}, 5.567 \times 10^{-6}$ (2.489×10^{-5})	$2.156 \times 10^{-5}, 6.321 \times 10^{-6}$ (2.788×10^{-5})	$1.913 \times 10^{-5}, 5.617 \times 10^{-6}$ (2.474×10^{-5})
$\frac{ U_1 }{ U_2 + cons.}$		$1.938 \times 10^{-5}, 1.543 \times 10^{-12}$	$1.948 \times 10^{-5}, 3.265 \times 10^{-13}$	$1.689 \times 10^{-5}, 6.666 \times 10^{-13}$
$\frac{ U_2 }{ U_1 + cons.}$		$5.654 \times 10^{-13}, 6.748 \times 10^{-6}$	$1.426 \times 10^{-12}, 6.947 \times 10^{-6}$	$1.055 \times 10^{-11}, 4.806 \times 10^{-6}$

Table II: The optimization results with different shaping schemes for broadband control fields under different objective functions. Here the symbols A, B mean that the phases at the resonant frequencies $\omega_1, \omega_2, \omega_3, \omega_4$ are fixed to zero or not, respectively, and $cons. = 10^{-8}$. The two numbers from left to right in each box correspond to $|U_1|$ and $|U_2|$, respectively. In the third row, values in the parentheses are the corresponding sum pathway amplitude $|U_1 + U_2|$.

3. Multi-block Scheme

The analysis above shows that the eight-block scheme is already quite effective at manipulating the pathway amplitude ratios. Here we will apply optimization schemes in which additional freedom is permitted to tailor the shape of laser pulses by dividing the spectrum into hundreds of evenly spaced blocks, as in recent pathway control experiments [19]. In our simulations, the spectral phases and amplitudes are taken to be zero everywhere except for the interval from 721 nm to 852 nm. The spectral bandwidth is divided into 640 evenly spaced blocks, and objective functionals are optimized by adjusting the phase of the 640 blocks. Two sub-schemes are considered. In multi-block scheme A the phases at the resonant frequencies ($\omega_1, \omega_2, \omega_3, \omega_4$) are always fixed to zero during the optimization as in the eight-block scheme, taking into account the considerations discussed in Refs. [22, 24]. On the other hand, in multi-block scheme B the phases at the resonant frequencies ($\omega_1, \omega_2, \omega_3, \omega_4$) are the same as the phases of the blocks they belong to, and are thus adjusted during the optimization process, which is also a common control procedure [19, 20]. The same finite difference-based gradient method is employed here for the numerical optimizations as well as the same five fitness functions in Table I are employed to assess the capability of the multi-block scheme for manipulating the quantum pathways. The results are shown in Table II. The sets of pathway amplitudes obtained by these schemes are very similar to those from the eight-block scheme, as seen in Table II. As mentioned above, the only difference between multi-block schemes A and B is whether or not the phases at the resonant frequencies $\omega_1, \omega_2, \omega_3, \omega_4$ are fixed to zero, with scheme A having the same condition that the phases at the four resonant frequencies are zero as the eight-block scheme. Accordingly, in our simulations, the phases of the blocks ($\omega_{reson} - \frac{d}{2}, \omega_{reson} + \frac{d}{2}$) centered at the resonant frequencies ω_{reson} are fixed to zero, and the resonant block widths (d) are narrower than the widths of the neighboring blocks. The sampling of the block boundaries in the simulations leads effectively to a situation in which there are actually four more phase variables in the spectral regions around the resonant frequencies in scheme A, because it permits the phases at the four resonant frequencies to differ from neighboring regions in the same spectral block. Therefore, scheme A has effectively a higher spectral resolution near the resonant frequencies which may explain why it performs better than scheme B. Compared with the eight-block scheme, multi-block scheme A has more phase control variables and thus gives larger amplitudes. The pathway amplitudes obtained by the multi-block scheme B are generally smaller than those corresponding to the eight-block scheme, which may be due to the amplitudes being much more sensitive to the phases closer to the resonant frequencies. Additionally, more freedom is available when the phases near the resonant frequencies have a higher spectral resolution, which can be achieved in many ways (e.g., Kumar *et al.* have shown high spectral resolution for control of the population amongst very close levels [27]). Thus, our results indicate that the eight-block scheme is an acceptable choice for manipulating the two quantum pathways, with multi-block scheme A only modestly improving the pathway amplitude ratio (approximately by 10%).

The four resonant frequencies have to be precisely known in the eight-block scheme and multi-block scheme A, which is not necessary in multi-block scheme B. In other words, additional information about the controlled system (e.g., the resonant frequencies) is used to design the first two schemes, which may explain why they perform better than multi-block scheme B. On the other hand, the multi-block scheme B is more generally applicable in a practical context, especially when little information is known about the quantum system under study.

IV. CONCLUSIONS AND DISCUSSIONS

The quantum control of pathway amplitudes in atomic Rubidium was theoretically investigated with a five-level model. Population was driven from the initial state $5S_{1/2}$ to the target state $5D_{3/2}$ through the two lowest-order available pathways: $5S_{1/2} \rightarrow 5P_{3/2} \rightarrow 5D_{3/2}$ (pathway 1), and $5S_{1/2} \rightarrow 5P_{1/2} \rightarrow 5D_{3/2}$ (pathway 2). By using a smooth field envelope along with non-resonant frequencies, the control fields in this work are more realistic than in a previous study [21]. For a narrowband control field with either Gaussian or rectangular envelopes, the observed oscillation period of the ratio between the two pathway amplitudes in the weak field regime corresponds to the detuning between transitions $5S_{1/2} \rightarrow 5P_{3/2}$ and $5P_{3/2} \rightarrow 5D_{3/2}$, which reflects the cooperation between the two pathways in order to maximize the population transfer. Furthermore, our analysis regarding the quantitative relationship between the oscillation parameters (i.e., the oscillation period and average value of $|U_1/U_2|$) and their relation to the system Hamiltonian indicates that HE-OD data could be employed for Hamiltonian identification [21]. For broadband control fields the pathway amplitudes are treated in the frequency domain. Several control schemes, namely a $\frac{\pi}{2}$ step scheme, an eight-block scheme and two multi-block schemes, are employed to manipulate the pathway dynamics. From the results of our simulations, the $\frac{\pi}{2}$ step scheme proposed by Silberberg [22] can increase the ratio between the two pathway amplitudes ($|U_1|/|U_2|$ or $|U_2|/|U_1|$) approximately by a factor of three (without directly controlling the interference between the two pathway amplitudes), while the other three schemes can increase the ratio by several orders of magnitude. The overall analysis indicates that the eight-block scheme with only four phase parameters is a practical choice for pathway manipulation in this five-level model due to its simplicity and effectiveness. The system investigated in this work has two intermediate states, corresponding to two 2nd-order pathways, whereas the procedures outlined here can be generalized to treat quantum systems involving more 2nd-order pathways in the low power regime when there are no higher order pathways present. In the high power regime, the simple linear relationship between the pathway amplitudes and $e^{i\varphi}$ (i.e., φ is a spectral block's phase) would be invalid because the dynamics are now described by a larger set of (higher order) terms in the Dyson expansion. In this latter case the multi-block scheme provides a more effective choice.

Acknowledgments

This work is supported by National Natural Science Foundation of China (Nos. 61203061, 61403362, 61374091 and 61473199). H.R. acknowledges the support from Chinese Academy of Sciences President's International Fellowship Initiative (No. 2015VTA008), and additional support from the US DOE (DE-FG02-02ER15344). R.R. acknowledges support from the US ARO (W911NF-13-1-0237).

-
- [1] J.M. Geremia, J. K. Stockton, H. Mabuchi, *Science*, 304, 270 (2004)
 - [2] H. M. Wiseman, A. C. Doherty, *Phys. Rev. Lett.* 94, 070405 (2005)
 - [3] H. Rabitz, R. de Vivie-Riedle, M. Motzkus, K. Kompa, *Science*, 288, 824 (2000)
 - [4] J. Combes, K. Jacobs, *Phys. Rev. Lett.* 96, 010504 (2006)
 - [5] G. G. Gillett, R. B. Dalton, B. P. Lanyon, M. P. Almeida, M. Barbieri, G. J. Pryde, J. L. O'Brien, K. J. Resch, S. D. Bartlett, A. G. White, *Phys. Rev. Lett.* 104, 080503 (2010)
 - [6] N. Yamamoto, H. I. Nurdin, M. R. James, I. R. Petersen, *Phys. Rev. A* 78, 042339 (2008)
 - [7] S. Mancini, H. M. Wiseman, *Phys. Rev. A* 75, 012330 (2007)
 - [8] S. B. Xue, R. B. Wu, W. M. Zhang, J. Zhang, C. W. Li, and T. J. Tarn, *Phys. Rev. A* 86, 052304 (2012)
 - [9] J. Zhang, Y.-X. Liu, F. Nori, *Phys. Rev. A* 79, 052102 (2009)
 - [10] Y. Silberberg, *Annu. Rev. Phys. Chem.* 60, 277 (2009);
 - [11] R. S. Judson and H. Rabitz, *Phys. Rev. Lett.* 68, 1500 (1992).
 - [12] H. M. Wiseman, *Phys. Rev. A* 49, 2133 (1994).
 - [13] A. Mitra and H. Rabitz, *Phys. Rev. A* 67, 033407 (2003)
 - [14] A. Mitra, I. R. Solá, H. Rabitz, *Phys. Rev. A* 67, 043409 (2003)
 - [15] A. Mitra, H. Rabitz, *J. Chem. Phys.* 125, 194107 (2006)
 - [16] A. Mitra, H. Rabitz, *J. Chem. Phys.* 128, 044112 (2008)
 - [17] A. Mitra, I. R. Solá, H. Rabitz, *Phys. Rev. A* 77, 043415 (2008)
 - [18] R. Rey-de-Castro, H. Rabitz, *Phys. Rev. A* 81, 063422 (2010)
 - [19] R. Rey-de-Castro, Z. Leghtas, H. Rabitz, *Phys. Rev. Lett.* 110, 223601 (2013)
 - [20] R. Rey-de-Castro, R. Cabrera, D. I. Bonder, H. Rabitz, *New J. Phys.* 15, 025032 (2013)
 - [21] F. Gao, R. Rey-de-Castro, A. M. Donovan, J. Xu, Y. Wang, H. Rabitz, F. Shuang, *Phys. Rev. A* 89, 023416 (2014)
 - [22] N. Dudovich, B. Dayan, S. M. Gallagher Faeder, Y. Silberberg, *Phys. Rev. Lett.* 86, 47 (2001)

- [23] M. C. Stowe, A. Pe'er, J. Ye, Phys. Rev. Lett. 100, 203001 (2008)
- [24] H. G. Lee, H. Kim, J. Lim, J. Ahn, Phys. Rev. A 88, 053427 (2013)
- [25] S. B. Bayram, M. Havey, M. Rosu, A. Sieradzan, A. Derevianko, W. R. Johnson, Phys. Rev. A 61, 050502 (2000)
- [26] Data of the energy levels and transition dipoles can be found in the website:
<http://www.steck.us/alkalidata/rubidium85numbers.pdf>
- [27] P. Kumar, S. A. Malinovskaya, V. S. Malinovsky, Phys. Rev. A 90, 033427 (2014)